2003

Full Cell Mathematical Model of a MCFC

N. Subramanian
University of South Carolina - Columbia

B. S. Haran
University of South Carolina - Columbia

Ralph E. White
University of South Carolina - Columbia, white@cec.sc.edu

Branko N. Popov
University of South Carolina - Columbia, popov@engr.sc.edu

Publication Info

Journal of the Electrochemical Society, 2003, pages A1360-A1367.

Journal of The Electrochemical Society, **150** (10) A1360-A1367 (2003)
0013-4651/2003/150(10)/A1360/8/$7.00 © The Electrochemical Society, Inc.

Full Cell Mathematical Model of a MCFC

N. Subramanian,* B. S. Haran, R. E. White,*** and B. N. Popov**,z**

Department of Chemical Engineering, University of South Carolina, Columbia, South Carolina 29208, USA

A theoretical model for the molten carbonate fuel cell was developed based on the three-phase homogeneous approach. Using this model, the contribution of different cell components to losses in cell performance has been studied. In general, at low current densities, the electrolyte matrix contributed to the major fraction of potential losses. Mass transfer effects became important at high current densities and were more prominent at the cathode. Electrolyte conductivity and cathode exchange current density seemed to play a limiting role in determining cell performance. Using the model, the maximum power density from a single cell for different cell thicknesses was determined.
 [DOI: 10.1149/1.1604786]

Manuscript submitted January 27, 2003; revised manuscript received April 20, 2003. Available electronically September 2, 2003.

Fuel cells convert chemical energy into electrical energy and have the advantage of continuous operation due to continuous supply of reactant gases. The high temperature molten carbonate fuel cell (MCFC) like any other fuel cell offers clean and efficient energy and is currently used in stationary power applications. The state-of-the-art MCFC includes NiO cathode, Ni-Cr anode, stainless steel (SS) current collectors and 32-68 mol % of Li_2CO_3/K_2CO_3 electrolyte held in $LiAlO_2$ matrix. Current research efforts are aimed at increasing the performance and the lifetime of the MCFC through development of better cell components.

Researchers interested in improving MCFC performance need to focus on cell components that have scope for yielding the maximum decrease in cell polarization. A full cell model would prove useful in analyzing the performance of MCFC in detail and in determining voltage losses in different regions of the cell. Previous modeling work in MCFC was focused on studying the performance of individual electrodes under different gas compositions and temperature. Yuh and Selman[1] modeled the performance of the MCFC cathode and anode and determined the dependencies of the electrode kinetic parameters on inlet gas composition. Other approaches to MCFC modeling have followed a similar methodology, and to date, no extensive full cell modeling has been done. Sampath *et al.*[2] used a linear current overpotential relationship in modeling the full cell performance. Wolf and Wilemski[3] used a two-dimensional (2-D) nonisothermal model to study the performance of MCFC. Machielse[4] used a simple algebraic model to describe the performance of the cell. The model does not consider any changes in reactant concentrations across the MCFC electrodes. A similar approach was used by Standaert *et al.*[5] to analyze the performance of the MCFC. They used two different forms of the Nernst equation to determine the cell potential. The first approximation considered the local current density to be constant (zero order approximation). The second took into account the nonhomogeneity of the current density by assuming that the local current density is a linear function of distance (first order approximation). Both of these approximations are valid only under limited cell operating conditions. A comprehensive full cell model is necessary to explain the fuel cell performance.

Previously, we developed a polarization model for the MCFC cathode based on volume averaging[6] of variables in the three phases separately. A similar approach has been used by Prins-Jansen *et al.*[7] to analyze the impedance of the MCFC cathode. This approach differs from the conventional agglomerate model used to analyze the performance of the MCFC anode[1] and cathode.[1] As compared to the agglomerate model[1] where macropores and micropores remain as separate entities. In this approach the pores in the electrode exist in a single continuum. Further, all three phases coexist within the porous electrode and reaction proceeds everywhere at the solid/melt interface. Hence, this model does not require any knowledge of measured values for film thickness and agglomerate radius.

The objective of this paper is to study the MCFC performance through theoretical modeling. To accomplish this we first derived model equations using a three-phase homogeneous model based on volume averaging. Next, the model equations were solved through finite element analysis and the polarization drops in different regions in the cell were determined. Finally, we analyzed the cell performance and studied the effect of different electrode variables on cell polarization. The maximum power that can be obtained was also determined for different cell thicknesses.

Model Development

A schematic of the MCFC modeled is shown in Fig. 1. CO_2 and O_2 enter the cathode, where CO_2 is reduced to CO_3^{2-}. H_2 enters the anode (along with a little amount of CO_2 to improve wetting of the electrode by the electrolyte) where CO_3^{2-} was oxidized to give back CO_2. Our full cell model extended the volume averaging approach we had used for the MCFC cathode to the anode and matrix regions. To begin with, we took a small volume element V. This volume should have been small compared to the overall dimensions of the porous electrode. But it should have been large enough to contain all three phases (gas, liquid, and solid). We defined meaningful local average properties based on this representative volume element. This volume was so chosen that adding pores around it did not result in a change in the local average properties. We avoided the bimodal pore distribution where we considered macropores to be filled with the gas and micropores to be occupied by the electrolyte. Pores of all sizes were filled with both the electrolyte and the gas, which was more realistic. A similar approach can also be used to model the matrix even though no gas phase was present there.

De Vidts and White[8] presented a detailed development of model equations for porous electrodes based on volume averaging, which has been adopted here. Detailed derivation of the mathematical equations in the cathode was presented in our previous paper.[6] Similar equations can be derived for the anode. In this paper we presented the final governing equations along with the boundary conditions in each of the cathode, anode and the matrix and their interfaces. Since the potential and the concentration varied significantly along the thickness of the fuel cell, a 1-D model was assumed. Further, we did not consider corrosion of the cathode and current collectors and assumed that the system was under steady state.

Equations at the current collector cathode interface ($x = 0$).— CO_2 and O_2 enter at the cathode side. The concentrations were equal to the inlet concentrations and the current was carried entirely by the electrons

$$u_{i,c}^{(l)} = 1,\ u_{i,c}^{(g)} = 1,\quad \sigma_c(\varepsilon_c^{(s)})^d \frac{\partial \langle \phi \rangle^{(s)}}{\partial x} = -I,$$

* Electrochemical Society Student Member.
** Electrochemical Society Active Member.
*** Electrochemical Society Fellow.
z E-mail: popov@engr.sc.edu

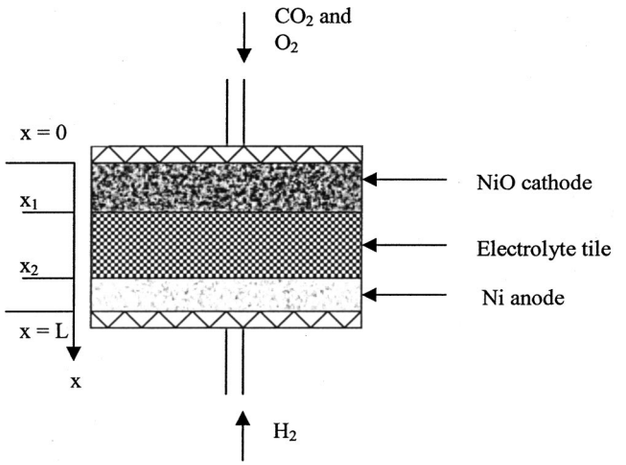

Figure 1. Schematic of the MCFC.

$$\kappa(\varepsilon_c^{(l)})^d \frac{\partial \langle\phi\rangle^{(l)}}{\partial x} = 0 \quad \text{where } i = CO_2, O_2 \qquad [1]$$

where $u_{i,c}$ refers to the dimensionless concentration of species i in the cathode. Notations for the rest of the symbols are given at the end of the paper.

Equations within the cathode region (from $x = 0$ to $x = x_1$).—

$$\frac{\partial}{\partial x}\left[D_{i,c}^{(l)}(\varepsilon_c^{(l)})^{b-1}\frac{\partial}{\partial x}(\varepsilon_c^{(l)}u_{i,c}^{(l)})\right] - \frac{a_c^{(lg)}k_{i,c}^{(lg)}}{K_{e,i,c}}(u_{i,c}^{(l)} - u_{i,c}^{(g)}) - \frac{s_{i,c}a_c^{(sl)}}{n_c F\langle c_i^*\rangle_c^{(l)}}\langle j_c\rangle^{(sl)} = 0 \qquad [2]$$

$$D_{i,c}^{(g)}\frac{\partial}{\partial x}\left[(\varepsilon_c^{(g)})^{b-1}\frac{\partial}{\partial x}(\varepsilon_c^{(g)}u_{i,c}^{(g)})\right] - D_{i,c}^{(g)}\frac{\partial}{\partial x} \times \left\{(\varepsilon_c^{(g)})^{b-1}\frac{u_{i,c}^{(g)}}{\langle c_{CO_2}^*\rangle_c^{(g)}u_{CO_2,c}^{(g)} + \langle c_{O_2}^*\rangle_c^{(g)}u_{O_2,c}^{(g)}}\frac{\partial}{\partial x} \times [\varepsilon_c^{(g)}(\langle c_{CO_2}^*\rangle_c^{(g)}u_{CO_2,c}^{(g)} + \langle c_{O_2}^*\rangle_c^{(g)}u_{O_2,c}^{(g)})]\right\} + a_c^{(lg)}k_{i,c}^{(lg)}(u_{i,c}^{(l)} - u_{i,c}^{(g)}) = 0 \qquad [3]$$

The following dimensionless variables were used in arriving at these equations

$$u_{i,k}^{(l)} = \frac{\langle c_i\rangle_k^{(l)}}{\langle c_i^*\rangle_k^{(l)}}, \quad u_{i,k}^{(g)} = \frac{\langle c_i\rangle_k^{(g)}}{\langle c_i^*\rangle_k^{(g)}}$$

where k represents the electrode, either the cathode or the anode and where $i = CO_2$, O_2, and $\langle j_c\rangle^{(sl)}$ is the local current density at the solid/liquid interface in the cathode given by the Butler Volmer (B-V) expression.

$$i_{0,c} = i_{0,c}^0(p_{CO_2,c}^*)^{r_{1,c}}(p_{O_2,c}^*)^{r_{2,c}} \qquad [5]$$

where $i_{0,c}$ and $i_{0,c}^0$ are the concentration dependent and concentration independent exchange-current densities respectively. The anodic and cathodic reaction orders $p_{1,c}, p_{2,c}$, and $q_{1,c}, q_{2,c}$ have values of -2, 0, -1, and 1/2, respectively. $r_{1,c}$ and $r_{2,c}$ have values of -1.25 and 0.375, respectively, for the peroxide mechanism.[9] These values will be different for other mechanisms. The charge balance gives the following equations for solid and liquid phase potentials.

$$\frac{\partial^2\langle\phi\rangle^{(s)}}{\partial x^2} = \frac{a_c^{(sl)}}{\sigma_c(\varepsilon_c^{(s)})^d}\langle j_c\rangle^{(sl)} \qquad [6]$$

$$\frac{\partial^2\langle\phi\rangle^{(l)}}{\partial x^2} = -\frac{a_c^{(sl)}}{\kappa(\varepsilon_c^{(l)})^d}\langle j_c\rangle^{(sl)} \qquad [7]$$

Equations at the cathode matrix interface ($x = x_1$).—In the matrix there were no species other than the electrolyte due to the assumption of zero gas crossover. This is a valid assumption because the allowable gas leakage was below 2% to avoid cell failure. So, the flux of all species was zero at the cathode/matrix interface. The liquid phase current was equal to the total current because the current was entirely carried by the ions.

$$\frac{\partial u_{i,c}^{(l)}}{\partial x} = 0$$

$$\left(\frac{\partial}{\partial x}(u_{i,c}^{(g)}) - \left\langle\frac{u_{i,c}^{(g)}}{\langle c_{CO_2}^*\rangle_c^{(g)}u_{CO_2,c}^{(g)} + \langle c_{O_2}^*\rangle_c^{(g)}u_{O_2,c}^{(g)}}\right\rangle\frac{\partial}{\partial x} \times (\langle c_{CO_2}^*\rangle_c^{(g)}u_{CO_2,c}^{(g)} + \langle c_{O_2}^*\rangle_c^{(g)}u_{O_2,c}^{(g)})\right) = 0$$

$$\kappa(\varepsilon_c^{(l)})^d\frac{\partial\langle\phi\rangle^{(l)}}{\partial x}\bigg|_{x=x_1^-} = \kappa(\varepsilon_s^{(l)})^{d_s}\frac{\partial\langle\phi\rangle^{(l)}}{\partial x}\bigg|_{x=x_1^+}$$

$$\sigma_c(\varepsilon_c^{(s)})^d\frac{\partial\langle\phi\rangle^{(s)}}{\partial x} = 0 \qquad [8]$$

where again $i = CO_2, O_2$.

Equations within the matrix (from $x = x_1$ to $x = x_2$).—There are no mass transport equations in the matrix due to the assumption that there was no gas crossover from one electrode to the other. Also, the gradient in the liquid phase potential remained constant (*i.e.*, the liquid phase current is equal to the total current). Hence

$$\kappa(\varepsilon_s^{(l)})^{d_s}\frac{\partial^2\langle\phi\rangle^{(l)}}{\partial x^2} = 0 \qquad [9]$$

The correction used for the conductivity, d_s is different from the correction d used in the electrodes.

Equations at the matrix anode interface ($x = x_2$).—The flux of all species is zero at the matrix/anode interface due to the assumption of no gas crossover. The liquid phase, current was equal to the

$$\langle j_c\rangle^{(sl)} = i_{0,c}\left\{\begin{array}{l}\left(\frac{\langle c_{CO_2}\rangle_c^{(l)}}{\langle c_{CO_2}^*\rangle_c^{(l)}}\right)^{p_{1,c}}\left(\frac{\langle c_{O_2}\rangle_c^{(l)}}{\langle c_{O_2}^*\rangle_c^{(l)}}\right)^{p_{2,c}}\exp\left(\frac{\alpha_{a,c}F(\langle\phi\rangle^{(s)} - \langle\phi\rangle^{(l)} - E_{eq,c})}{RT}\right) \\ -\left(\frac{\langle c_{CO_2}\rangle_c^{(l)}}{\langle c_{CO_2}^*\rangle_c^{(l)}}\right)^{q_{1,c}}\left(\frac{\langle c_{O_2}\rangle_c^{(l)}}{\langle c_{O_2}^*\rangle_c^{(l)}}\right)^{q_{2,c}}\exp\left(\frac{-\alpha_{c,c}F(\langle\phi\rangle^{(s)} - \langle\phi\rangle^{(l)} - E_{eq,c})}{RT}\right)\end{array}\right\} \qquad [4]$$

total current similar to the cathode/matrix interface.

$$\frac{\partial u_{i,a}^{(l)}}{\partial x} = 0$$

$$\left\{ \frac{\partial}{\partial x}(u_{i,a}^{(g)}) - \left\langle \frac{u_{i,a}^{(g)}}{\langle c_{CO_2}^{*}\rangle_a^{(g)} u_{CO_2,a}^{(g)} + \langle c_{H_2}^{*}\rangle_a^{(g)} u_{H_2,a}^{(g)}} \right\rangle \frac{\partial}{\partial x} \right\} = 0$$

$$\times \left(\langle c_{CO_2}^{*}\rangle_a^{(g)} u_{CO_2,a}^{(g)} + \langle c_{H_2}^{*}\rangle_a^{(g)} u_{H_2,a}^{(g)} \right)$$

$$\kappa(\varepsilon_s^{(l)})^{d_s} \frac{\partial \langle\phi\rangle^{(l)}}{\partial x}\bigg|_{x=x_2^-} = \kappa(\varepsilon_a^{(l)})^{d} \frac{\partial \langle\phi\rangle^{(l)}}{\partial x}\bigg|_{x=x_2^+}$$

$$\sigma_a(\varepsilon_a^{(s)})^{d} \frac{\partial \langle\phi\rangle^{(s)}}{\partial x} = 0 \qquad [10]$$

where $i = CO_2, H_2$

Equations within the anode (from $x = x_2$ to $x = L$).—

$$\frac{\partial}{\partial x}\left[D_{i,a}^{(l)} (\varepsilon_a^{(l)})^{b-1} \frac{\partial}{\partial x}(\varepsilon_a^{(l)} u_{i,a}^{(l)}) \right] - \frac{a_a^{(lg)} k_{i,a}^{(lg)}}{K_{e,i,a}} (u_{i,a}^{(l)} - u_{i,a}^{(g)}) + \frac{s_{i,a} a_a^{(sl)}}{n_a F \langle c_i^{*}\rangle_a^{(l)}} \langle j_a\rangle^{(sl)} = 0 \qquad [11]$$

$$D_{i,a}^{(g)} \frac{\partial}{\partial x}\left[(\varepsilon_a^{(g)})^{b-1} \frac{\partial}{\partial x}(\varepsilon_a^{(g)} u_{i,a}^{(g)}) \right] - D_{i,a}^{(g)} \frac{\partial}{\partial x} \times \left\{ (\varepsilon_a^{(g)})^{b-1} \frac{u_{i,a}^{(g)}}{\langle c_{CO_2}^{*}\rangle_a^{(g)} u_{CO_2,a}^{(g)} + \langle c_{H_2}^{*}\rangle_a^{(g)} u_{H_2,a}^{(g)}} \frac{\partial}{\partial x^{*}} \times \left[\varepsilon_a^{(g)} (\langle c_{CO_2}^{*}\rangle_a^{(g)} u_{CO_2,a}^{(g)} + \langle c_{H_2}^{*}\rangle_a^{(g)} u_{H_2,a}^{(g)}) \right] \right\} + a_a^{(lg)} k_{i,a}^{(lg)} (u_{i,a}^{(l)} - u_{i,a}^{(g)}) = 0 \qquad [12]$$

where $i = CO_2, H_2$ and $\langle j_a\rangle^{(sl)}$ is the local current density at the solid/liquid interface in the anode given by

$$\langle j_a\rangle^{(sl)} = i_{0,a} \left\{ \begin{array}{l} \left(\frac{\langle c_{CO_2}\rangle^{(l)}}{\langle c_{CO_2}^{*}\rangle^{(l)}} \right)^{p_{1,a}} \left(\frac{\langle c_{H_2}\rangle^{(l)}}{\langle c_{H_2}^{*}\rangle^{(l)}} \right)^{p_{2,a}} \\ \quad \times \exp\left(\frac{\alpha_{a,a} F(\langle\phi\rangle^{(s)} - \langle\phi\rangle^{(l)} - E_{eq,a})}{RT} \right) \\ -\left(\frac{\langle c_{CO_2}\rangle^{(l)}}{\langle c_{CO_2}^{*}\rangle^{(l)}} \right)^{q_{1,a}} \left(\frac{\langle c_{H_2}\rangle^{(l)}}{\langle c_{H_2}^{*}\rangle^{(l)}} \right)^{q_{2,a}} \\ \quad \times \exp\left(\frac{-\alpha_{c,a} F(\langle\phi\rangle^{(s)} - \langle\phi\rangle^{(l)} - E_{eq,a})}{RT} \right) \end{array} \right\} \qquad [13]$$

$$i_{0,a} = i_{0,a}^{0} (p_{CO_2,a}^{*})^{r_{1,a}} (p_{H_2,a}^{*})^{r_{2,a}} (p_{H_2O,a}^{*})^{r_{3,a}} \qquad [14]$$

In the anode the mechanism suggested by Ang and Sammells and as adopted by Lu and Selman is considered.[10] For this mechanism $p_{1,a}, p_{2,a}$, and $q_{1,a}, q_{2,a}$ have values of 0, 1/2, and 1, −1/2, respectively. $r_{1,a}$, $r_{2,a}$ and $r_{3,a}$ have a value of 0.25 each. Moreover, the activity of water was assumed to be unity in deriving Eq. 13 and 14. The governing equations for solid and liquid phase potentials are similar to the cathode

$$\frac{\partial^2 \langle\phi\rangle^{(s)}}{\partial x^2} = \frac{a_a^{(sl)}}{\sigma_a (\varepsilon_a^{(s)})^{d}} \langle j_a\rangle^{(sl)} \qquad [15]$$

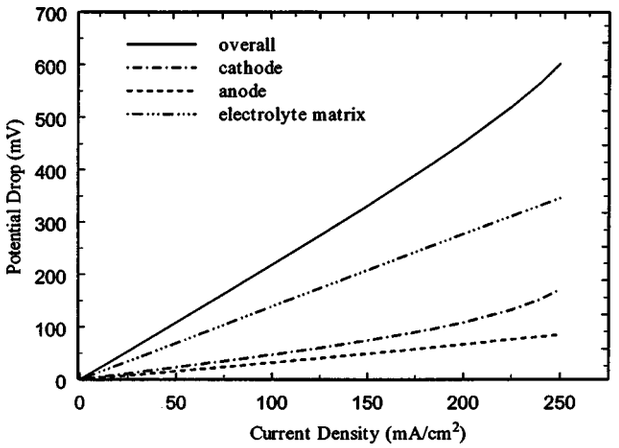

Figure 2. Comparison of overpotentials in different cell components with the overall polarization.

$$\frac{\partial^2 \langle\phi\rangle^{(l)}}{\partial x^2} = -\frac{a_a^{(sl)}}{\kappa(\varepsilon_a^{(l)})^{d}} \langle j_a\rangle^{(sl)} \qquad [16]$$

Equations at the anode current collector interface ($x = L$).— CO_2 and H_2 enter at the anode. The concentrations are equal to the inlet concentrations and the current is carried entirely by the electrons similar to the cathode/current collector interface

$$u_{i,a}^{(l)} = 1, u_{i,a}^{(g)} = 1, \sigma_a (\varepsilon_a^{(s)})^{d} \frac{\partial \langle\phi\rangle^{(s)}}{\partial x} = -I, \kappa(\varepsilon_a^{(l)})^{d} \frac{\partial \langle\phi\rangle^{(l)}}{\partial x} = 0 \qquad [17]$$

where again $i = CO_2, H_2$.

Results and Discussion

There are eight unknowns, namely, solution phase potential ($\langle\phi\rangle^{(l)}$), solid phase potential ($\langle\phi\rangle^{(s)}$), dimensionless concentration in the liquid, and the gas phases for the three components ($u_{i,k}^{(g)}$ and $u_{i,k}^{(l)}$, respectively in the electrode k, k = c or a; for species i, i = CO_2, O_2, or H_2). The set of governing equations and boundary conditions 1-17 were solved for these eight variables using FEMLAB 2.2 and the results arediscussed in the following section. Model simulations were run with the set of parameters given in Table I. The equilibrium potentials in the cathode, $E_{eq,c}$ and the anode, $E_{eq,a}$ were 0.0 and −1.02 V, respectively, with respect to oxygen reduction on gold. Cell potential was calculated from the difference in solid phase potentials at $x = 0$ and $x = L$ *i.e.*, $V = \langle\phi\rangle^{(s)}|_0 - \langle\phi\rangle^{(s)}|_L$. Overall potential drop was determined by finding the deviation of the cell potential from equilibrium potential ($V_{eq} - V$). The potential drop in the cathode, electrolyte matrix, and the anode were the overpotentials $E_{eq,c} - (\langle\phi\rangle^{(s)}|_0 - \langle\phi\rangle^{(l)}|_{x_1})$, $\langle\phi\rangle^{(l)}|_{x_1} - \langle\phi\rangle^{(l)}|_{x_2}$, and $E_{eq,a} - (\langle\phi\rangle^{(l)}|_{x_2} - \langle\phi\rangle^{(s)}|_L)$, respectively. The cell potential determined using model simulations might be different from the experimental values due to resistance in current collectors. But the model is based on the assumption that the resistance in the current collectors is negligible.

In MCFC, the main property of interest is the cell polarization under different applied loads. A clear understanding of the contribution of different cell components to the cell polarization is necessary. Figure 2 shows the potential drop in the cathode, anode, electrolyte tile (matrix), and the overall potential drop. It is obvious that the potential drop in the cathode and anode was smaller compared to the overall potential drop, implying that there was a huge potential drop in the matrix. This is attributed to the ohmic loss in the electrolyte. This agrees with what has been reported in literature[12] where they

claim that 70% of the total cell ohmic losses occur in the electrolyte. Also, as the current density increased, the percentage potential drop in the matrix decreased and the losses in the matrix and rest of the fuel cell became comparable as represented in Fig. 3. The percentage increase in the cell potential drop with the current density was more in the cathode than in the matrix (a higher exponential dependence of the potential drop on current density in the cathode than in the matrix). This can be attributed to the concentration polarization in the electrodes, which increased exponentially with increasing current density (the upward bending effect due to mass transfer limitations).

The potential drop in the matrix is seen clearly by plotting the liquid phase potentials in the cathode, matrix, and the anode as shown in Fig. 4. It can be seen that there is a big jump in the liquid phase potential in the matrix. Similarly, a considerable potential drop is seen in the cathode while the potential remains almost the same in the anode. Also, as the applied current density increases this jump in the liquid phase potential increases both in the matrix and the cathode. In the electrolyte matrix the potential drop is uniform across the matrix. However, in the cathode there is a sudden drop in potential close to the cathode/matrix interface. In both the cathode and the anode, change in solid phase potential was negligible because the electronic conductivity was high. However, the liquid phase potential changed significantly with current density. Because $\langle\phi\rangle^{(l)}$ increased and $\langle\phi\rangle^{(s)}$ remained the same, the overpotential increased ($\langle\phi\rangle^{(s)} - \langle\phi\rangle^{(l)}$) leading to a drop in cell potential.

Figure 5 shows the potential drop for varying matrix thickness at different applied current densities. Potential drop increased with matrix thickness as well as current density. However, as the current density increased the slope of potential drop *vs.* matrix thickness increased. This suggests that decreasing the matrix thickness will improve the performance of MCFC. This has been observed by previous researchers.[12] They found that the voltage drop (ΔV_{ohm}) followed a linear trend with the thickness (*i.e.*, $\Delta V_{ohm} = 0.533t$). But there are practical constraints to decreasing the matrix thickness. Continuous dissolution of the NiO cathode material occurs in the electrolyte. If the matrix thickness is small then Ni^{2+} diffusion from the cathode to the anode is easier and the cell is shorted in a short span of time. This leads to a decrease in the life of the fuel cell. Hence a compromise must be made between the life of the fuel cell and the cell performance while choosing the matrix thickness.

Figure 6 presents the cell potential for different applied current densities. There are two cases shown, case 1 with concentration effects and case 2 assuming negligible concentration gradients. Case 1 takes into account the concentration gradients in the gas and the liquid phase along with potential gradients and activation losses. Case 2 considers only the potential gradients and activation losses

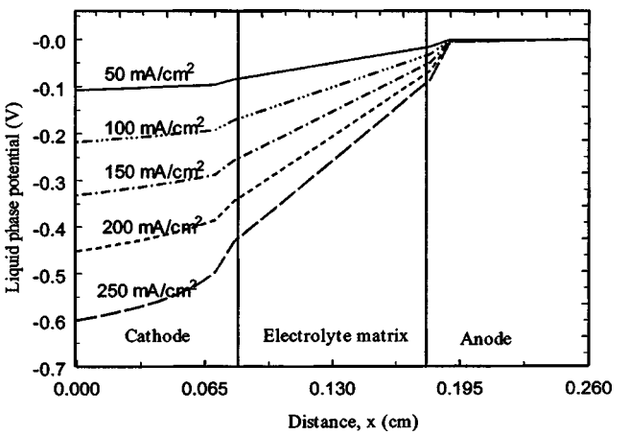

Figure 4. Liquid phase potential profiles across the cell at different current densities.

and neglects concentration gradients both in the liquid phase and the solid phase. A small difference in the cell potentials is observed between the two different cases at low current densities. As the current density increased this difference increased. This is because at low current densities ohmic effects dominated and mass transfer effects were negligible. But as the current density increased, there was mixed control (ohmic and mass transfer). Figure 7 shows the plot of concentration polarization for different current densities, which increased exponentially with increasing current densities. Concentration polarization is calculated by finding the difference in polarizations between the two cases. At low current densities the rate of the reaction is low and the reactant concentrations are very near to the inlet concentrations. But as the current density increases more of the reactants get consumed and the concentration decreases. Hence concentration polarization increased as the current density increased. Plotting overpotential *vs.* current density showed a linear curve for case 2 and an upward bending curve for case 1. This upward bending effect was due to mass transfer limitations and has been discussed in the simulations of the cathode model.[6] The matrix thickness in this simulation was 0.1 cm. But changing the matrix thickness did not change the concentration polarization. That was because of the assumption that there was no gas crossover and hence there was no gas going into the matrix. Changes in the concentrations did not affect the potential drop in the matrix. The entire concentration polarization lay mainly in the cathode and its value increased with increase in current densities. Hence, to model the

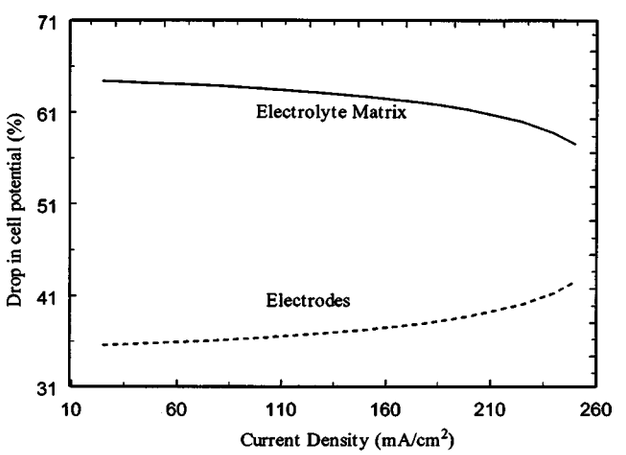

Figure 3. Comparison of potential losses in the electrolyte matrix and the electrodes.

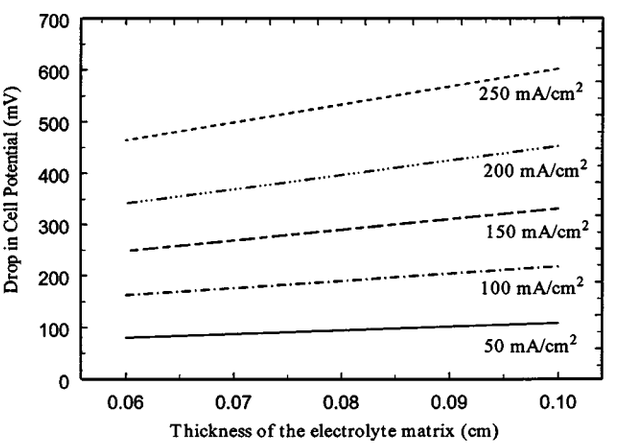

Figure 5. Potential drop as a function of electrolyte matrix thickness for different current densities.

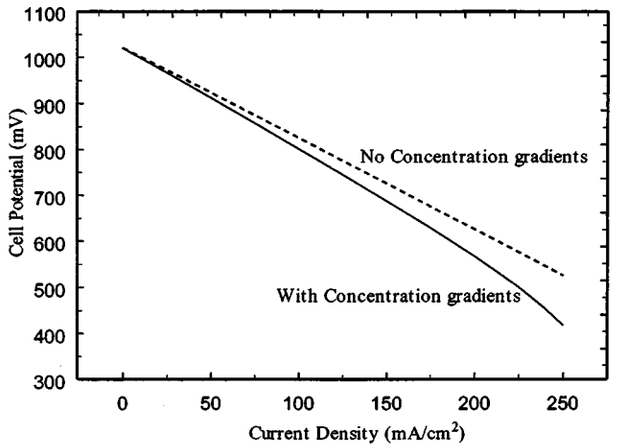

Figure 6. Comparison of the cell potentials obtained using the two models (with and without concentration gradients).

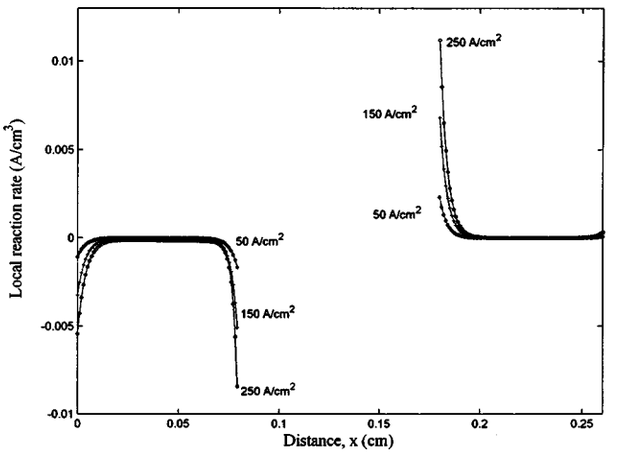

Figure 8. Local current density in the cathode and the anode for different applied current densities. Dashed lines with + markers represent 50 mA/cm^2; dashed lines with no markers represent 150 mA/cm^2; dashed lines with O markers represent 250 mA/cm^2.

system accurately, concentration gradients had to be taken into account. Figure 7 also shows the effect of electrolyte conductivity κ on concentration polarization; it shows that the concentration polarization was large for low electrolyte conductivities. At high current densities for low values of κ, a significant potential drop occurred close to the cathode/matrix interface as seen in Fig. 4. This led to a more nonuniform reaction distribution. In this case, the reaction rate and hence the local current density at the matrix/cathode interface was high. Mass transfer becomes limiting at such high reaction rates and hence concentration polarization was high at low electrolyte conductivities.

The local current density profiles are given in Fig. 8. The electrolyte conductivity was kept at 1.0 S/cm during these simulations. The local current density remained almost the same throughout the cathode except near the matrix and the current collectors. This suggests that most of the reaction occurred at the current collector/cathode and cathode/matrix interfaces. When the applied current density was increased, this nonuniformity in the local current density increased more. The same was observed in the anode though here most of the reaction occurred at the matrix/anode interface. This suggests that we cannot use a constant local current density along the whole length of the electrode *i.e.*, the zero order approximation given by Standaert *et al.*[5] to model the system. Also the local current density cannot be assumed to vary linearly as can be seen clearly from Fig. 8. So, the first order approximation suggested by Standaert *et al.*[5] is also not true. In the cathode, the cathodic part of the current density from the B-V equation was high compared to the anodic part. Hence, we observed a negative local current density. In the anode, the anodic term is high leading to a positive local current density. This can be seen clearly in the simulation results.

We next analyze the effect of electrode parameters namely exchange current density and electrode conductivity on the cell performance. Different electrode materials have different exchange current densities; cathode materials: NiO − 0.81 mA/cm^2 [13] −50 mA/cm^2,[6] $LiCoO_2$ − 0.53 mA/cm^2 [13] −5 mA/cm^2,[6] $LiNiCoO_2$ − 0.65 mA/cm^2;[6] and anode material: Ni 110 mA/cm^2. Simulations were run for different exchange current densities of the cathode keeping all other parameters constant. The same was done in the anode. The results are shown in Fig. 9 and 10. Electrolyte conductivity κ was kept at 0.02 S/cm in the simulations of these two figures. As can be seen from Fig. 9, the cell voltage increased sharply when the cathode exchange current density ($i^0_{0,c}$) was increased from 0.1 to 1 mA/cm^2 and increased again until $i^0_{0,c}$ is around 10 mA/cm^2. But above 10 mA/cm^2, increasing $i^0_{0,c}$ did not affect the cell potential. This is the case for any applied current density although the cell potentials vary with the applied currents. The same was observed with the anode exchange current density $i^0_{0,a}$ as shown in Fig. 10.

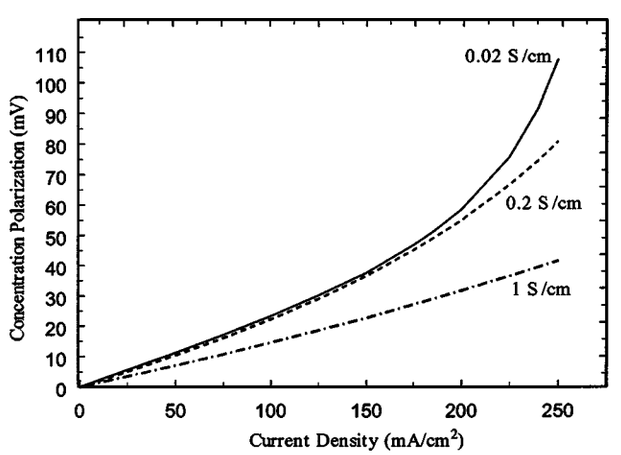

Figure 7. Concentration polarization for different ionic conductivities. The polarization is the difference between the cell potentials obtained in Fig. 6.

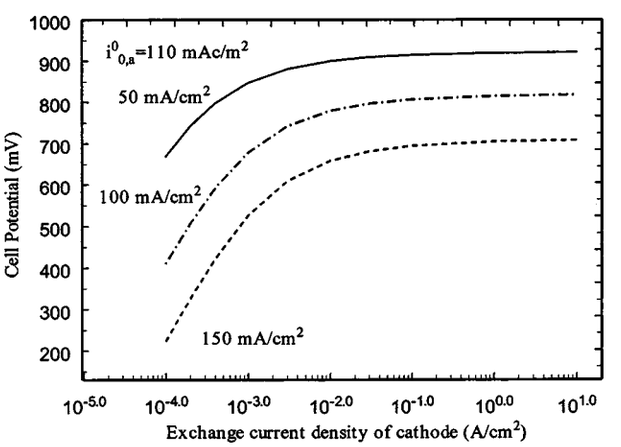

Figure 9. Cell potential as a function of the cathodic exchange current density.

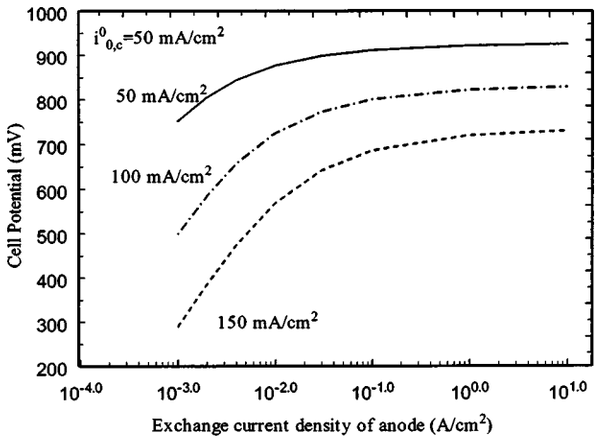

Figure 10. Cell potential as a function of the anodic exchange current density.

This is because at low values of $i^0_{0,c}$, the system was under kinetic limitations of the cathode. As $i^0_{0,c}$ increased, cathode kinetics was no longer the limiting factor and other phenomena controlled the performance (mass transfer or ohmic or mixed control). The electrode conductivities showed a similar behavior. Figure 11 shows the effect of cathode conductivity on cell potential. Below 1 S/cm any decrease in the cathode conductivity decreased the cell potential drastically. The cell was already under limitations due to the low electrolyte conductivity of 0.02 S/cm. Any decrease in the cathode conductivity added to the ohmic limitation and resulted in a sudden decrease in the cell performance. For cathode conductivities greater than 1 S/cm, the decrease in cell potential was negligible. The state-of-the-art cathode materials have the following conductivities; NiO, 13S/cm;[6] $LiCoO_2$, 1S/cm;[6] $LiNiCoO_2$, 5S/cm;[6] and $LiFeO_2$, 0.05 S/cm.[13] This suggests that $LiFeO_2$ will suffer from ohmic limitations. Figure 12 shows the effect of electrolyte conductivity on performance. The behavior was similar to electrode conductivity and exchange current density. The cell potential follows an asymptotic profile with increasing electrolyte conductivity at all applied currents. From 0.02 to 0.2 S/cm there was a wide difference in cell

Table I. List of parameters used in model simulations.[11]

Parameter	Value	Reference
Diffusion coefficient of CO_2 in the liquid phase in cathode, $D^{(l)}_{CO_2,c}$	$1e^{-3}$ cm^2/s	7
Diffusion coefficient of O_2 in the liquid phase in cathode, $D^{(l)}_{O_2,c}$	$3e^{-3}$ cm^2/s	7
Diffusion coefficient of CO_2 in the liquid phase in anode, $D^{(l)}_{CO_2,a}$	$1e^{-3}$ cm^2/s	
Diffusion coefficient of H_2 in the liquid phase in anode, $D^{(l)}_{H_2,a}$	$1e^{-3}$ cm^2/s	
Diffusion coefficient of CO_2 in the gas phase in cathode, $D^{(g)}_{CO_2,c}$	1.16 cm^2/s	11
Diffusion coefficient of O_2 in the gas phase in cathode, $D^{(g)}_{O_2,c}$	1.16 cm^2/s	11
Diffusion coefficient of CO_2 in the gas phase in anode, $D^{(g)}_{CO_2,a}$	4.625 cm^2/s	11
Diffusion coefficient of O_2 in the gas phase in anode, $D^{(g)}_{H_2,a}$	4.625 cm^2/s	11
Cathode conductivity, σ_c	13 S/cm	13
Electrolyte conductivity, κ	2.0×10^2 S/cm	7
Correction for diffusion coefficient, b	1.5	8
Correction for conductivity, d	1.5	8
Correction for conductivity in the electrolyte matrix, d_s	-3.6	
Rate constant of the molar flux of CO_2 between the liquid and gas phase in the cathode, $k^{(lg)}_{CO_2,c}$	3×10^3 cm/s	8
Rate constant of the molar flux of O_2 between the liquid and gas phase in the cathode, $k^{(lg)}_{O_2,c}$	2×10^3 cm/s	8
Rate constant of the molar flux of CO_2 between the liquid and gas phase in the anode, $k^{(lg)}_{CO_2,c}$	3×10^3 cm/s	8
Rate constant of the molar flux of H_2 between the liquid and gas phase in the anode, $k^{(lg)}_{H_2,a}$	2×10^3 cm/s	8
Thickness of the fuel cell, L	0.26 cm	Measured
Thickness of the cathode, x_1	0.08 cm	Measured
Thickness of the matrix, $x_2 - x_1$	0.1 cm	Measured
Thickness of the anode, $L - x_2$	0.08 cm	Measured
Liquid porosity in the cathode, $\varepsilon^{(l)}_c$	0.3	Measured
Gas porosity in the cathode, $\varepsilon^{(g)}_c$	0.4	Measured
Solid porosity in the cathode, $\varepsilon^{(s)}_c$	0.3	Measured
Liquid porosity in the anode, $\varepsilon^{(l)}_a$	0.2	Measured
Gas porosity in the anode, $\varepsilon^{(g)}_a$	0.45	Measured
Solid porosity in the anode, $\varepsilon^{(s)}_a$	0.35	Measured
Liquid porosity in the electrolyte matrix, $\varepsilon^{(l)}_s$	0.7	Measured
Cathodic transfer coefficient in the cathode, $\alpha_{c,c}$	0.5	9
Anodic transfer coefficient in the cathode, $\alpha_{a,c}$	1.5	9
Cathodic transfer coefficient in the anode, $\alpha_{c,a}$	1.5	1
Anodic transfer coefficient in the anode, $\alpha_{a,a}$	0.5	1
$r_{1,c}$	-1.25	9
$r_{2,c}$	0.375	9
$r_{1,a}$	0.25	1
$r_{2,a}$	0.25	1
Equilibrium potential of the cathodic reaction $E_{eq,c}$, V	0	
Equilibrium potential of the anodic reaction $E_{eq,a}$, V	-1.02	

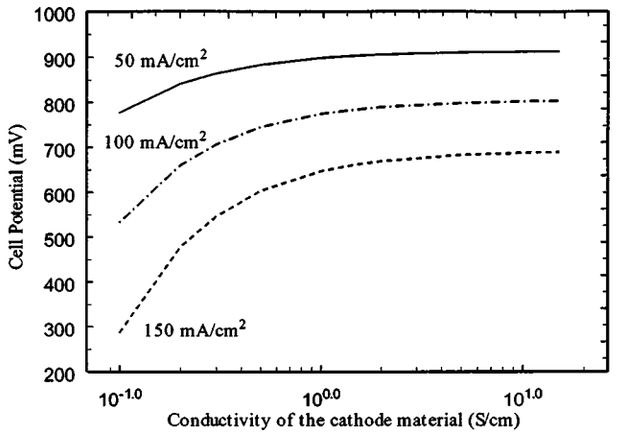

Figure 11. Effect of cathode conductivity on cell potential.

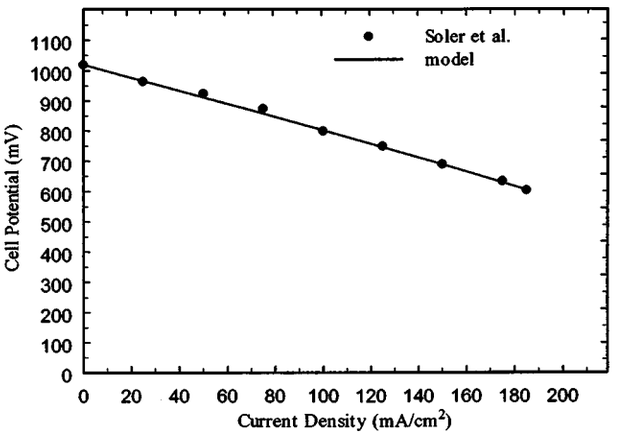

Figure 13. Comparison of model to experimental data.

potentials. But from 0.2 to 1 S/cm the cell potential increased slightly. Thus, trying to increase the electrolyte conductivity to 0.2 S/cm for a given set of cathode and anode materials improved the performance of the full cell.

Figure 13 shows the results of the model simulation along with the experimental data of Soler *et al.*[14] The parameters used in the cathode were taken from the previous paper[6] where the cathode model was fitted to the experimental data. The anode data was fitted separately before attempting to fit the full cell data. The cathode and anode parameters used in the model simulation are given in Table I. In the cathode and anode the effective electrolyte conductivity was calculated using the Bruggeman formula. ($\kappa_{eff} = \kappa\varepsilon^{1.5}$). We were not able to fit the data using such a relation in the matrix. An effective conductivity greater than the one estimated by the Bruggeman relation has to be used in the matrix to fit the model to the experimental data. Doyle *et al.*[15] reported a similar dependence of the effective conductivity in the plasticized electrolyte in a plastic lithium-ion cell (where they reported a conductivity less than that predicted by the Bruggeman relation) though the Bruggeman formula held good in the cathode and the anode.

In the MCFC, the cell potential varied linearly with the applied current density. This was observed both in the model simulations and the experimental data. This was expected because the activation polarization observed in low temperature fuel cells at low current densities vanishes in high temperature cells.

Next, note how the power density changed with increasing load for different cell thickness as shown in Fig. 14. Power density is defined as the product of the applied current density and the voltage. The plot shows that the maximum power density was obtained around an applied load of 220 mA/cm^2 for a cell thickness of 0.26 cm. At low current densities, the power density increased as the current density increased. But above 220 mA/cm^2, power density did not increase due to increase in polarization losses. Hence the curve went through a maximum. When the thickness was decreased, the maximum power density increased. This is attributed to the reduction in ohmic and concentration polarization due to reduced thickness. Thus, reducing the thickness increased the optimum power density and enabled operation at higher power densities. Note that in practice, the point of maximum power density does not correspond to optimum power density, because at that point, the internal heat generation would have been high and undesirable for fuel cell operation. Hence the fuel cell is operated at much lower power densities.

Conclusions

We developed a three-phase homogeneous model based on volume averaging to analyze the performance of the MCFC. The simulation results are summarized below.

1. Most of the potential drop was due to ohmic resistances especially in the matrix. The potential drop in the matrix was confirmed by the huge drop in the liquid phase potentials in the matrix. The combined potential drop in the two electrodes becames comparable to that in the matrix at high current densities. This is mainly due to the increase in concentration polarization in the cathode.

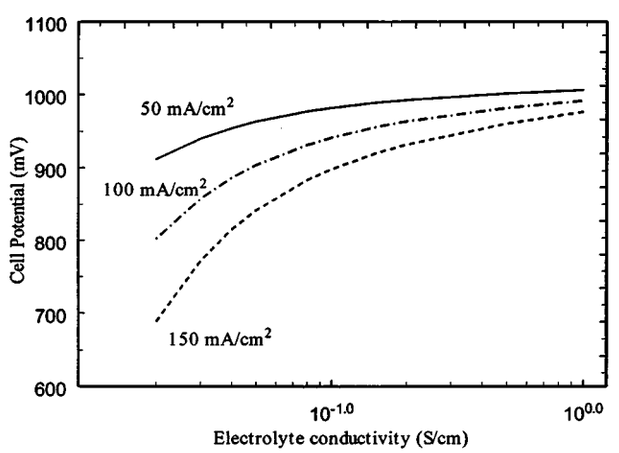

Figure 12. Effect of electrolyte conductivity on cell potential.

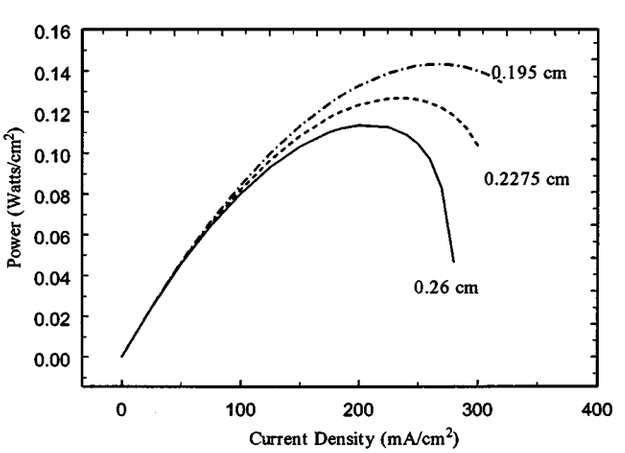

Figure 14. Power density *vs.* current density for varying cell thickness.

2. Concentration polarization effects became important at high current densities. Concentration polarization mainly exists in the cathode and was affected by electrode design parameters such as porosity, electrolyte filling, and active surface area. Hence it is important to take into account the effects of mass transfer while modeling the system.

3. The local current density in the cathode and anode is nonuniform. This nonuniformity increased as the applied current density increased.

4. Matrix thickness played a critical role in determining cell performance. Reducing the thickness improved the performance but reduced the life of the fuel cell. Hence a compromise must be made between these two opposing phenomena while choosing the electrolyte matrix thickness.

5. Electrolyte conductivity and cathode exchange current density were the limiting factors for cell performance. Future efforts should be directed to increase these parameters.

6. In the MCFC, the cell potential varied linearly with the applied current density because the activation polarization observed in low temperature fuel cells at low current densities vanished in high temperature cells. The maximum power density does not necessarily correspond to optimum power density, as the heat generation at current densities leading to such power densities is very high and undesirable for the fuel cell operation.

Acknowledgment

Financial support by the National Energy Technology Laboratory (NETL), which is supported by the U.S. Department of Energy (DOE), is gratefully acknowledged.

The University of South Carolina assisted in meeting the publication costs of this article.

List of Symbols

a	specific surface area, cm^2/cm^3
b	correction for diffusion coefficient
$\langle c \rangle$	volume averaged concentration, mol/cm^3
$\langle c^* \rangle$	volume averaged bulk concentration, mol/cm^3
d	correction for conductivity in the electrodes
d_s	correction for conductivity in the electrolyte matrix
D	diffusion coefficient, cm^2/s
E_{eq}	equilibrium potential, V
F	faraday's constant, 96487 C/equiv
i_0^0	concentration independent exchange current density, A/cm^2
i_0	concentration dependent exchange current density, A/cm^2
I	applied current, A/cm^2
$\langle j_k \rangle^{(sl)}$	average local current density due to reaction occurring in electrode k at the liquid/solid interface, A/cm^2
$k_{i,k}^{(lg)}$	rate constant of molar flux of species i between the liquid and gas phase in electrode k, cm/s
$K_{e,i,k}$	equilibrium constant relating the concentration of species i in the liquid and gas phase in electrode k, $\langle c_i^* \rangle^{(l)} / \langle c_i^* \rangle^{(g)}$
L	thickness of the fuel cell, cm
n	no. of electrons transferred in reaction
p^*	equilibrium partial pressure, relative to total pressure
R	gas constant, J/mol/K
S	stoichiometric coefficient
u	dimensionless concentration
x_1	cathode/matrix interface
x_2	matrix/anode interface

Greek

α_c	cathodic transfer coefficient
α_a	anodic transfer coefficient
$\langle \phi \rangle^{(l)}$	liquid phase potential, V
$\langle \phi \rangle^{(s)}$	solid phase potential, V
ε	porosity
κ	electrolyte conductivity, S/cm
σ	electrode conductivity, S/cm

Subscripts and Superscripts

a	anode
c	cathode
(g)	gas phase
i	species i = CO_2, O_2, H_2, or H_2
k	electrode
(l)	liquid phase
(lg)	liquid/gas interface
s	electrolyte matrix
(s)	solid phase
(sl)	solid/liquid interface

References

1. C. Y. Yuh and J. R. Selman, *J. Electrochem. Soc.*, **131**, 2062 (1984).
2. V. Sampath, A. F. Sammells, and J. R. Selman, *J. Electrochem. Soc.*, **127**, 79 (1980).
3. T. L. Wolf and G. Wilemski, *J. Electrochem. Soc.*, **130**, 48 (1983).
4. L. A. H. Machielse, in *Modeling of Batteries and Fuel Cells*, R. E. White, M. W. Verbrugge, and J. F. Stockel, Editors, PV 91-10, p. 166, The Electrochemical Society Proceedings Series, Pennington, NJ (1991).
5. F. Standaert, K. Hemmes, and N. Woudstra, *J. Power Sources*, **63**, 221 (1996).
6. N. Subramanian, B. S. Haran, P. Ganesan, R. E. White, and B. N. Popov, *J. Electrochem. Soc.*, **150**, A46 (2003).
7. J. A. Prins-Jansen, J. D. Fehribach, K. Hemmes, and J. H. W. de Wit, *J. Electrochem. Soc.*, **143**, 1617 (1996).
8. P. de Vidts, Ph.D. Thesis, Texas A & M University, College Station, TX (1995).
9. J. Prins-Jansen, Ph.D. Thesis, Delft University of Technology, Netherlands, (1996).
10. S. H. Lu and J. R. Selman, *J. Electrochem. Soc.*, **136**, 1068 (1989).
11. E. L. Cussler, *Diffusion, Mass Transfer in Fluid Systems*, Cambridge University Press, New York (1984).
12. J. H. Hirschenhofer, D. B. Stauffer, R. R. Engleman, and M. G. Klett, *Fuel Cell Handbook*, 4th ed., Chap. 4, U.S. Department of Energy/Federal Energy Technology Center, Morgantown, WV (1998).
13. G. L. Lee, J. R. Selman, and L. Pomp, *J. Electrochem. Soc.*, **140**, 390 (1993).
14. J. Soler, T. Gonzalez, M. J. Escudero, T. Rodrigo, and L. Daza, *J. Power Sources*, **4650**, 1 (2002).
15. M. Doyle, J. Newman, A. S. Gozdz, C. N. Schmutz, and J.-M. Tarascon, *J. Electrochem. Soc.*, **143**, 1890 (1996).